Biallelic splicing variants in the nucleolar 60S assembly factor RBM28 cause the ribosomopathy ANE syndrome

Carson J. Bryant[a,1], Cláudia F. Lorea[b,1], Hiram Larangeira de Almeida Jr[c], Letícia Weinert[d], Leonardo Vedolin[e], Filippo Pinto e Vairo[f,g,2,3], and Susan J. Baserga[a,h,i,2,3]

[a]Department of Molecular Biophysics and Biochemistry, Yale School of Medicine, New Haven, CT 06520; [b]Children's Care Unit of the Teaching Hospital, Federal University of Pelotas, CEP 96030-000, Pelotas–Rio Grande do Sul, Brazil; [c]Dermatology Department, Federal University of Pelotas, CEP 96030-000, Pelotas–Rio Grande do Sul, Brazil; [d]Endocrinology Department, Federal University of Pelotas, CEP 96030-000, Pelotas–Rio Grande do Sul, Brazil; [e]Diagnósticos da América, São Paulo - SP, 05425-020, Brazil; [f]Center for Individualized Medicine, Mayo Clinic, Rochester, MN 55905; [g]Department of Clinical Genomics, Mayo Clinic, Rochester, MN 55905; [h]Department of Genetics, Yale School of Medicine, New Haven, CT 06520; and [i]Department of Therapeutic Radiology, Yale School of Medicine, New Haven, CT 06520

Edited by Nahum Sonenberg, McGill University, Montreal, QC, Canada, and approved March 29, 2021 (received for review November 2, 2020)

Alopecia, neurologic defects, and endocrinopathy (ANE) syndrome is a rare ribosomopathy known to be caused by a p.(Leu351Pro) variant in the essential, conserved, nucleolar large ribosomal subunit (60S) assembly factor RBM28. We report the second family of ANE syndrome to date and a female pediatric ANE syndrome patient. The patient presented with alopecia, craniofacial malformations, hypoplastic pituitary, and hair and skin abnormalities. Unlike the previously reported patients with the p.(Leu351Pro) *RBM28* variant, this ANE syndrome patient possesses biallelic precursor messenger RNA (pre-mRNA) splicing variants at the 5′ splice sites of exon 5 (ΔE5) and exon 8 (ΔE8) of *RBM28* (NM_018077.2:c.[541+1_541+2delinsA]; [946G > T]). In silico analyses and minigene splicing experiments in cells indicate that each splice variant specifically causes skipping of its respective mutant exon. Because the ΔE5 variant results in an in-frame 31 amino acid deletion (p.(Asp150_Lys180del)) in *RBM28* while the ΔE8 variant leads to a premature stop codon in exon 9, we predicted that the ΔE5 variant would produce partially functional RBM28 but the ΔE8 variant would not produce functional protein. Using a yeast model, we demonstrate that the ΔE5 variant does indeed lead to reduced overall growth and large subunit ribosomal RNA (rRNA) production and pre-rRNA processing. In contrast, the ΔE8 variant is comparably null, implying that the partially functional ΔE5 RBM28 protein enables survival but precludes correct development. This discovery further defines the underlying molecular pathology of ANE syndrome to include genetic variants that cause aberrant splicing in *RBM28* pre-mRNA and highlights the centrality of nucleolar processes in human genetic disease.

ANE syndrome | ribosomopathy | ribosome biogenesis | RBM28

Ribosome biogenesis (RB) is the essential cellular process in which the complex macromolecular ribosomal machinery is manufactured and assembled, enabling protein translation (1–4). Both ribosomal RNA (rRNA) and ribosomal protein (RP) components must be correctly synthesized, processed, modified, folded, translocated, and ultimately joined in the cytoplasm to engage in global protein synthesis (1–3). For eukaryotes, four rRNA molecules (1, 5) and about 80 RPs (1, 6, 7) form the core of the mature small (40S) and large (60S) ribosomal subunits. The demand for ribosomes during the cell cycle is immense: in a growing yeast cell, more than 30 ribosomes are synthesized per second (8), while in a growing HeLa cell, this figure balloons to 125 ribosomes per second (9). Over 200 trans-acting assembly factors are necessary to achieve the fast and accurate ribosome assembly required to meet this tremendous cellular translational demand (1).

Given that up to 80% of cellular metabolism is devoted to RB (10), it is unsurprising that defects in RB factors are causative of a class of human diseases known as ribosomopathies (1, 11–16). Though not fully understood, tissue-specific defects are the hallmark of ribosomopathies (11, 17). Tissues formed from hematopoietic or neural crest cell lineages are disproportionately affected, resulting in anemia, neutropenia, and leukemia, bone marrow failure diseases including Diamond–Blackfan Anemia (DBA) (18–23) and Shwachman–Diamond syndrome (24–26), craniofacial, dermatological, and neurological diseases including Treacher Collins syndrome (27–29) and postaxial acrofacial dysostosis (30), and alopecia, neurologic defects, and endocrinopathy (ANE) syndrome (31–34).

ANE syndrome (OMIM: 612079) (31, 35) is a rare ribosomopathy defined by heterogeneous clinical features of variable severity including alopecia, neurological deformities, intellectual disability, and hormonal deficiencies with pubertal delay. In the only ANE syndrome case report published to date, Nousbeck and coworkers studied five brothers of consanguineous parentage with variable ANE syndrome features, finding that ANE syndrome patient tissue samples had quantifiably fewer ribosomes and qualitatively dysmorphological rough endoplasmic reticula versus healthy control samples (31). All five patients were found to carry a homozygous missense variant (p.(Leu351Pro); L > P) in *RBM28* (31), a known essential 60S assembly factor orthologous to yeast

Significance

RBM28 is a human protein essential for proper assembly of the large ribosomal subunit, crucially enabling synthesis of all cellular proteins. Defects in RBM28 cause rare ribosomopathies: alopecia, neurological defects, and endocrinopathy (ANE) syndrome. We investigated an ANE syndrome patient with a clinical presentation consistent with the definition of ANE syndrome but possessing differing genetic variants and molecular pathology. We find one inherited allele is null, clarifying that ANE syndrome is not caused by *RBM28* haploinsufficiency, while the other inherited allele retains enough function to enable survival but preclude proper development. Our results define an underlying pathology of ANE syndrome, further delineating an emerging class of assembly factor ribosomopathies and underscoring the importance of nucleolar processes in human health.

Author contributions: C.J.B., C.F.L., F.P.e.V., and S.J.B. designed research; C.J.B., C.F.L., H.L.d.A., L.W., L.V., and F.P.e.V. performed research; C.J.B. contributed new reagents/analytic tools; C.J.B., F.P.e.V., and S.J.B. analyzed data; and C.J.B., C.F.L., F.P.e.V., and S.J.B. wrote the paper.

The authors declare no competing interest.

This article is a PNAS Direct Submission.

See online for related content such as Commentaries.

[1]C.J.B. and C.F.L. contributed equally to this work.

[2]F.P.e.V. and S.J.B. contributed equally to this work.

[3]To whom correspondence may be addressed. Email: vairo.filippo@mayo.edu or susan.baserga@yale.edu.

This article contains supporting information online at https://www.pnas.org/lookup/suppl/doi:10.1073/pnas.2017777118/-/DCSupplemental.

Published May 3, 2021.

Nop4 (36–39). Follow-up studies further defined the clinical extent of endocrinopathy (32) and the biochemical mechanisms of hair and skin defects (33) and of inhibited ribosome biogenesis (34, 40) due to impaired function of RBM28 or its yeast homolog, Nop4. However, due to the rarity of the disease and lack of sufficient animal model studies, further investigation of ANE syndrome has been limited.

We report a female pediatric patient in the second family of ANE syndrome to date, unrelated to the family in the original case report (31). The ANE syndrome patient has a clinical presentation consistent with the definition of ANE syndrome but possesses differing genetic variants and molecular pathology. Using in vivo techniques, we demonstrate that the patient's compound heterozygous splicing variants in *RBM28* create one hypomorphic (ΔE5) and one null (ΔE8) allele with respect to overall growth and 60S pre-rRNA processing functions. By elucidating the pathology of an ANE syndrome patient, our results bolster and extend our understanding of this rare ribosomopathy and reinforce the importance of proper nucleolar function in human health and disease.

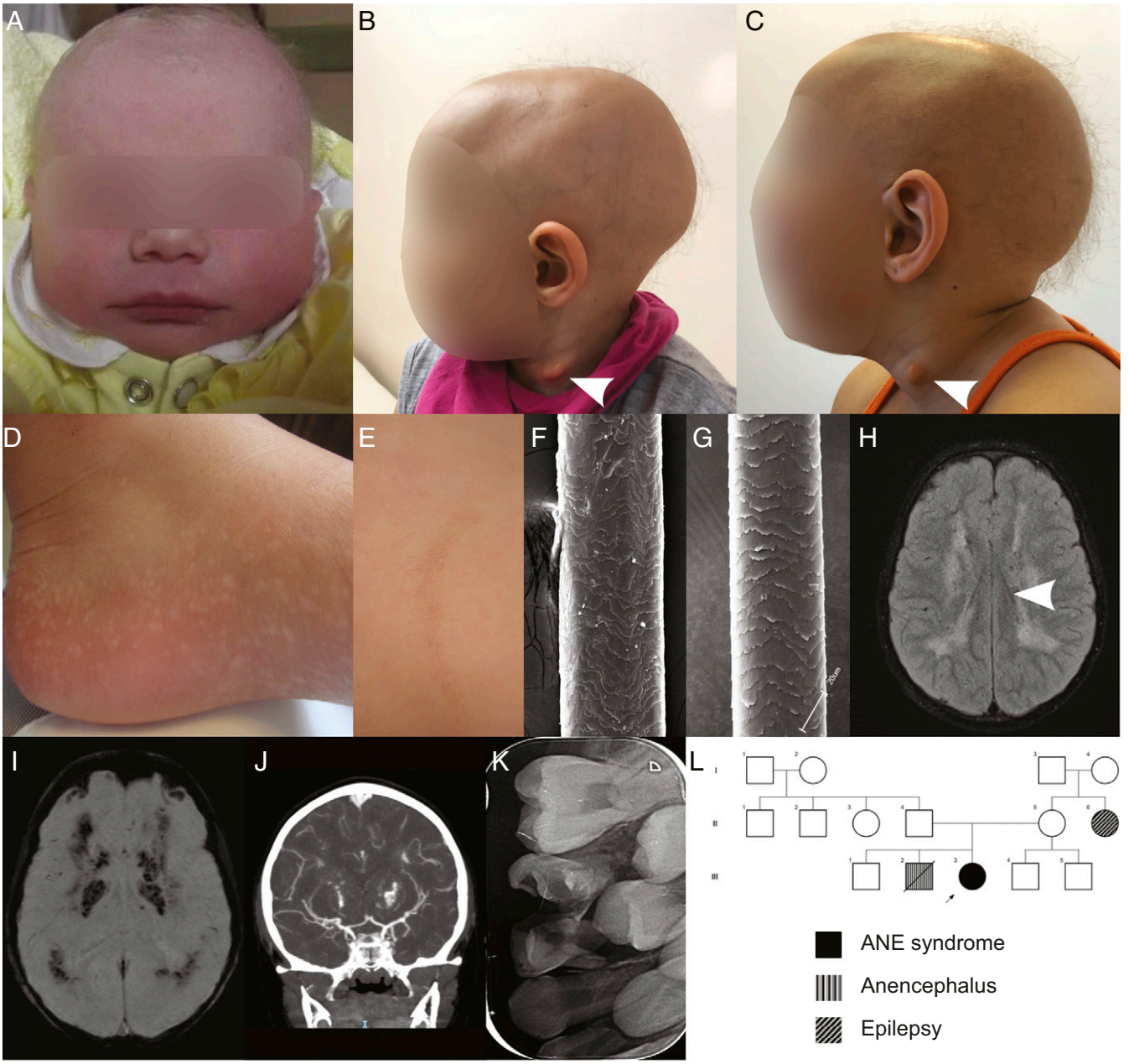

Fig. 1. Clinical presentation and analysis of a female pediatric ANE syndrome patient. (*A*) Patient during the newborn period. (*B* and *C*) Patient at 3 y (*B*) and 6 y (*C*) of age. Note the sparse hair, branchial cleft cyst on the neck (white arrowhead), and prominent ears. (*D* and *E*) Dermatological features including acral guttate hypomelanosis on the feet (*D*) and verrucous nevus on the right scapular region (*E*). (*F* and *G*) Scanning electron microscopy of a hair from the patient (*F*), which displays an irregular hair cuticle, versus a normal control hair (*G*). Micrographs were imaged with 500× magnification. (*H*) Fluid-attenuated inversion recovery image showing diffuse white matter lesions and periventricular cysts (arrowhead). (*I*) Susceptibility weighted imaging MRI indicating diffuse calcifications affecting basal ganglia and subcortical white matter. (*J*) Angiotomography image showing middle cerebral artery stenosis and presence of collateral circulation. (*K*) Premolars with double roots. (*L*) Patient family pedigree. One of the proband's siblings (III-2) died in utero diagnosed with anencephaly; no necropsy or genetic testing was performed.

Results

A Female Pediatric Patient with Alopecia, Neurologic Defects, and Endocrinopathy (ANE) Syndrome Possesses Biallelic Splicing Variants in *RBM28*. A Brazilian girl was born at term to nonconsanguineous parents with a birth weight of 2,735 g (fifth percentile), head circumference (HC) of 32 cm (second percentile), and Apgar score 10/10. No delays were noted in the first months of life. She started babbling at 12 mo of age, and she walked at 16 mo. Her weight and height remained steadily at the fifth percentile. She was born with sparse hair that fell out in the following few days and has not regrown. On physical examination, she has a branchial cleft cyst and mild facial dysmorphism including prominent ears and very few sparse terminal hairs (Fig. 1 *A*–*C*). We observed dermatological features including an unexpected guttate hypomelanosis on the feet resembling idiopathic guttate hypomelanosis seen in adults in sun-exposed areas (Fig. 1*D*) and a verrucous nevus accompanied by hypertrichosis on the right scapular region (Fig. 1*E*). Patient hairs examined using scanning electron microscopy displayed a very irregular cuticle (Fig. 1*F*) when compared to normal control hairs with a regular distribution of cuticular scales (Fig. 1*G*).

The patient also presented with aberrant brain features but normal metabolite and endocrine levels. At 4 y of age, a brain MRI with proton spectroscopy was performed and showed a slightly hypoplastic anterior hypophysis, mild volumetric reduction of white matter, small cysts in frontal and parietal white matter, and diffuse symmetric predominantly supratentorial and subcortical leukoencephalopathy with surrounding calcifications (Fig. 1 *H* and *I*). Proton spectroscopy was considered normal. At 6 y of age, brain vascular malformations were evidenced by computed angiotomography (Fig. 1*J*). Chromosomal microarray and metabolic testing including biotinidase activity, plasma amino acids, urinary organic acids, and plasma acylcarnitines profiling were essentially normal. Endocrinological evaluation was first performed at 3 y of age. She was at the 10th percentile for height (predicted height was at the 25th percentile), her growth velocity was 6 cm/year, and she had prepubertal sexual characteristics. Bone age was 2 y and 10 mo when the chronological age was 3 y and 10 mo (bone age was projected at the 50th percentile of the stature growth chart). Full morning pituitary hormonal tests were normal, and a stimulation test with 1 μg adrenocorticotropic hormone excluded adrenal insufficiency. Pituitary hormone reevaluations at 4, 5, and 6 y of age also yielded normal results (*SI Appendix*, Table S1). Her growth velocity has been 6 cm/year the last 3 y. Parathyroid hormone and calcium metabolism were also evaluated, and results were considered normal for the patient's age.

A follow-up evaluation indicated the patient had persistent craniofacial and neurological defects. At 6 y of age, she had been treated for six dental caries, and she had two teeth broken due to bruxism. Tooth root malformations were observed after dental extractions (Fig. 1*K*). She has microcephaly (HC = 48.3 cm; < third percentile), limited speech capacity, and no sphincter control. She is very active but has underdeveloped fine motor skills. No other family members were identified with the same phenotype. It was her mother's fifth pregnancy but the third from this couple (Fig. 1*L*). The second pregnancy of this couple was interrupted due to anencephaly; the fetus was male and did not undergo any genetic testing (Fig. 1*L*).

Considering the patient's complex phenotype, whole exome sequencing was performed and revealed compound heterozygous variants in *RBM28* (NM_018077.2:c.[541+1_541+2delinsA];[946G > T]). The first variant occurs in the canonical 5′ splice site of exon 5 and is classified as pathogenic following the American College of Medical Genetics and the Association for Molecular Pathology joint guidelines (41) (Fig. 2 *A*, *Top Left*). While the second variant was initially classified as a variant of uncertain significance [NP_060547.2:p.(Ala316Ser)] and deemed benign or tolerated by PolyPhen2 (42) and SIFT (43), this variant is predicted to negatively impact splicing by the SpliceAI algorithm (44) due to its location at the 5′ splice site of ΔE8 (Fig. 2 *A*, *Top Right*). Each variant allele was inherited from an unaffected parent as confirmed by Sanger sequencing, and neither variant was present in population-based databases including gnomAD (45). After taking the patient's clinical features and *RBM28* genotype into consideration, she was ultimately diagnosed with ANE syndrome. Table 1 compares characteristics of this patient to those previously reported (31).

In Silico Predictions and In Vivo Splicing Assays Show That Patient *RBM28* Splice Variants Ablate Wild-Type Splicing. The ANE syndrome patient has biallelic splicing variants at exon 5 and exon 8 of *RBM28*, which disrupt nucleotides in the 5′ splice site consensus sequence (46) that are conserved in wild-type (WT) *RBM28*. The GT deleted from the exon 5 splice donor (ΔE5) corresponds to the invariant GT in the 5′ splice site consensus sequence (Fig. 2 *A*, *Top Left*), while the G > T variant in exon 8 (ΔE8) alters the highly conserved G at the IVS−1 position (Fig. 2 *A*, *Top Right*). The relative locations of each variant, the exons and protein domains of RBM28, and its well-conserved yeast ortholog Nop4 (26% identity) are also illustrated in Fig. 2*A*. Because splice site sequence is essential for proper pre-mRNA processing and downstream translation of the RBM28 protein, we sought to discover what new or aberrant patterns of splicing might occur in the presence of either variant. In the absence of patient transcriptomic or proteomic data, we utilized both computational splicing prediction software packages and in vivo minigene splicing assays to determine the outcomes of the *RBM28* ΔE5 or ΔE8 splicing variants.

In silico splicing prediction algorithms predicted that the 5′ splice site functionality of each of the ΔE5 and ΔE8 variants is severely impaired, and that only the ΔE5 variant allele is likely to retain residual function. Overall, four different computational metrics [calculated with SpliceAI (44), Human Splicing Finder (47), and AnalyzerSpliceTool (48)] predicted that each patient variant will negatively impact the function of the corresponding WT *RBM28* 5′ splice site (Fig. 2*A*, inset tables). We hypothesize that each variant will disrupt WT splicing of exons 5 and 8 to the downstream exon, and any splicing that does occur will most likely use a different 5′ splice site. Furthermore, holistic analysis of potential substituting splice sites using NNSplice (49) and COSSMO (50) (Dataset S1) predicted five possible ΔE5 substitute splice sites that would create an in-frame partial deletion; these are predicted to be functional. In contrast, all predicted ΔE8 substitute splice sites would contain premature termination codons, rendering ΔE8 a nonfunctional allele.

In order to determine which of the predicted substitute splice events predominate in vivo, we conducted minigene splicing assays in human HEK-293 cells followed by RT-PCR and sequencing analysis (Fig. 2*B*). Wild-type minigene constructs predominately resulted in the expected WT-spliced product containing three exons (Fig. 2*C*, lanes 3 and 7). For the WT exon 8 construct, we also observed a minor band resulting from retention of intron 7 (Fig. 2*C*, lane 7). Strikingly, ΔE5 and ΔE8 minigene constructs caused a complete shift from WT-spliced products to splice products that cleanly skipped the variant exons (Fig. 2*C*, lanes 4 and 8). This observation was experimentally verified in triplicate (*SI Appendix*, Fig. S1*A*). Since splice events upstream of exon 4 were predicted for the ΔE5 variant allele (Dataset S1), a longer minigene fragment spanning exon 1 through exon 6 was also analyzed for substitute splice events upon incorporation of the ΔE5 variant (*SI Appendix*, Fig. S1*B*). Splicing of the WT exon 1-6 minigene was normal, and introduction of the ΔE5 variant caused specific exon 5 skipping in the final splice product, consistent with results from the shorter minigene (*SI Appendix*, Fig. S1*B*). The splice event observed for the ΔE5 variant corresponds to the

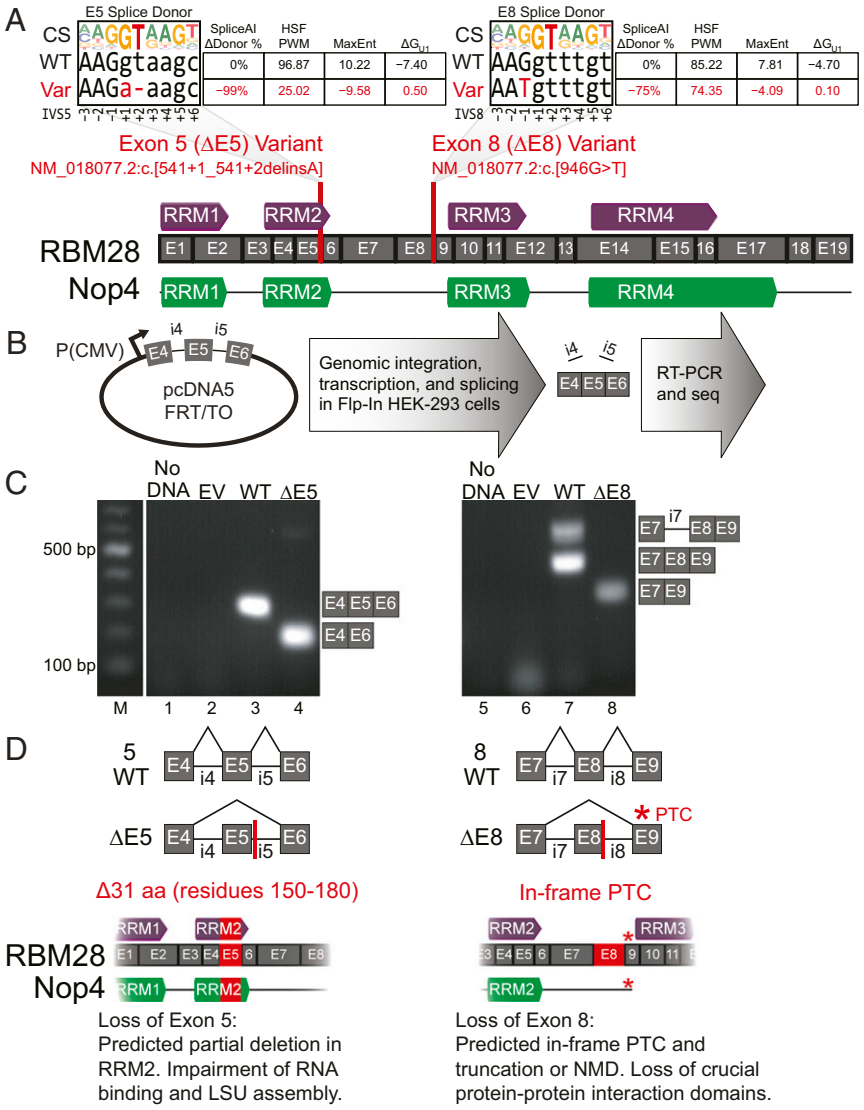

Fig. 2. In silico analyses and cellular minigene splicing assays reveal that only the ΔE5 variant *RBM28* allele will have residual function. (*A*) Computational splicing prediction algorithms predict that patient variants negatively impact the function of the WT 5′ splice site. Analysis of 5′ splice site function without and with patient variant at ΔE5 (*Left*) or ΔE8 (*Right*). 5′ splice site consensus sequence (46) is shown above WT and variant (Var, red) sequences at each exon's 5′ splice site. Exonic nucleotides (IVS−3 to IVS−1) are capitalized, and intronic nucleotides (IVS+1 to IVS+6) are in lowercase. Splicing algorithm scores are tabulated for SpliceAI (SpliceAI ΔDonor %), HumanSplicingFinder position weight matrices (HSF PWM), maximum entropy (MaxEnt), and free energy of base pairing to the U1 snRNA (ΔG, AnalyzerSpliceTool). 5′ splice sites are considered broken if the decrease in SpliceAI Donor %, PWM, or MaxEnt scores upon mutation exceeds a variation threshold (>50% decrease for SpliceAI Donor %, >10% decrease for PWM, >30% decrease for MaxEnt) or if the ΔG of U1 snRNA base pairing is unfavorable ($\Delta G_{U1} > 0$). (*Bottom*) Location of exons (gray), RNA recognition motif (RRM) protein domains (purple or green), and patient variants (red) at exons 5 and 8 in human *RBM28* and yeast Nop4. (*B*) Schematic of minigene splicing assay for a generic transcript containing three exons and two introns. The gene fragment of interest (minigene, gray) was cloned into the cytomegalovirus (CMV) expression cassette of the pcDNA5/FRT/TO vector. After genomic integration into HEK-293 Flp-In T-REx cells, the fragment is transcribed and spliced by the cellular machinery. Total RNA is isolated and analyzed by RT-PCR and sequencing. (*C*) RT-PCR and sequencing results of WT and variant (Var) ΔE5 and ΔE8 minigene constructs. WT and patient variant *RBM28* minigenes were constructed from a genomic library clone using PCR and site-directed mutagenesis. Spliced transcripts were amplified from total cDNA and separated by agarose gel electrophoresis. No DNA (Lanes 1 and 5) and empty pcDNA5/FRT/TO vector (EV, Lanes 2 and 6) PCR controls were run. Sequencing results are diagrammed to the right of each image. M, 1 kb+ ladder marker. (*D*) Deleterious effects on proteins translated from patient variant transcripts. Location of exons (gray), RRM protein domains (purple and green) for RBM28 and Nop4, and variant positions (red). (*Left*) Skipping ΔE5 creates an in-frame partial deletion of RRM2, which is predicted to impair RNA binding and LSU assembly. Critical protein interaction domains necessary for LSU biogenesis are retained (RRM3 and RRM4). (*Right*) Skipping ΔE8 creates a frame shift and PTC (red asterisk) in exon 9, resulting in protein truncation or mutant transcript degradation via nonsense-mediated decay. Critical protein interaction domains necessary for LSU biogenesis are lost (RRM3 and RRM4).

predicted partial deletion splice (Δ31, removing amino acids 150 to 180) in *SI Appendix*, Fig. S1*A* (Dataset S1 [ID 5.08]). Surprisingly, the ΔE8 skipping event was not predicted by NNSplice or COSSMO, although it would still create a premature termination codon (PTC) in exon 9 and cause protein truncation or nonsense-mediated degradation (NMD) of the transcript.

Only the ΔE5 Patient Variant Allele Retains Residual Function in 60S rRNA Biogenesis in Yeast. Since RBM28 and its well-conserved yeast homolog Nop4 have been shown to be essential in human CRISPR knockout screens (51–53), animal models (54), and in yeast (36, 37), we reasoned that the ANE syndrome patient must possess some gene product functionality from the *RBM28* locus.

Table 1. Comparison of clinical characteristics with previously reported cases

	Nousbeck et al. (31)	This report
Sex	Male (5/5)	Female
Age (years)	20–39	4
Intellectual deficiency	+	+
Alopecia/hypotrichosis	+	+
Microcephaly	3/5	+
Dental caries	+	+
Hypodontia	3/5	Not present at this time
Limb contractures	4/5	—
Central adrenal insufficiency	5/5	Not present at this time
Brain MRI	Hypoplastic pituitary (only performed in one patient)	Hypoplastic pituitary and other findings described in the text
Branchial cleft cyst	—	+
Hypochromic spots	—	+

Taken together, these results led us to hypothesize that the ΔE8 variant allele has minimal functional potential and is effectively null, while the ΔE5 variant allele retains residual functional potential and is likely hypomorphic. This model is consistent with the observation that each variant allele was inherited from different unaffected parents, assuming that development of ANE syndrome only occurs when total RBM28 function is less than 50% of the wild type.

To test the hypothesis that the ΔE5 variant is hypomorphic and the ΔE8 variant is null, we constructed a yeast model in which loss of endogenous yeast Nop4 function could be tested for growth complementation by variant Nop4 or the orthologous RBM28 proteins (Fig. 3*A*). Previously, the yeast homolog of human RBM28 known as Nop4 was used to study the impact of the classical Leu > Pro (L > P) ANE syndrome mutation on 60S biogenesis and on the large ribosomal subunit (LSU) processome network (34). Nop4 and RBM28 were reported to be 26% identical and contain four aligning RNA recognition motif (RRM) domains (34). For completeness, we tested the functionality of both Nop4 and RBM28 variant proteins in the absence of endogenous Nop4. The variant proteins for RBM28 were generated directly from the coding sequence, while Nop4 variant proteins were rationally designed by alignment (Fig. 3*B* and Dataset S2). For each wild-type protein, previously generated L > P variants mirroring the original case report were utilized (Leu306Pro in Nop4 and Leu351Pro in RBM28) (31, 34), while ΔE5 and ΔE8 deletion variants were generated by Gibson cloning. Variant protein coding sequences were shuttled into the expression cassette of the p414-GPD vector, which is driven by the glyceraldehyde-3-phosphate dehydrogenase (GPD) promoter. Plasmids were transformed into a previously constructed *P(GAL)::3HA-NOP4* strain, for which endogenous HA-tagged Nop4 expression is repressed in dextrose-containing media, while FLAG-tagged rescue protein variants are constitutively expressed regardless of carbon source (Fig. 3*A*). We biochemically verified that each strain exhibited carbon source–dependent expression of endogenous HA-Nop4 and carbon source–independent expression of extrachromosomal FLAG-tagged variant proteins via immunoblot (Fig. 3*C*).

We assayed the ability of each variant protein to restore vegetative growth in the absence of endogenous Nop4. We chose to rescue at the optimal yeast growth temperature (30 °C) as well as at temperatures both lower (17 °C and 23 °C) and higher (37 °C) than the optimum. Because RB is an energy intensive, kinetically limited process (1, 55), restricting ambient energy via temperature decrease exacerbates any subtle defects that might exist between wild-type and mutant proteins, facilitating defect detection (cold sensitive). Investigation of a higher temperature enabled us to detect the extent to which variants were energetically destabilized compared to the wild-type conformational fold (temperature sensitive).

First, we examined the functionality of WT and variant Nop4 proteins. Tenfold serial dilutions of strains on solid media illustrate that coexpression of endogenous Nop4 with all of the Nop4 constructs did not alter normal vegetative growth at 30 °C, indicating no dominant negative effects on growth of the variant Nop4 proteins (Fig. 3*D*, panel 1). Furthermore, WT, L > P, and ΔE5 variants of Nop4 largely support vegetative growth in the absence of endogenous Nop4 function, while empty vector (EV) plasmids or ΔE8 Nop4 exhibit severe growth defects at all temperatures examined (Fig. 3*D*, panels 2–5). The Nop4 ΔE5 variant was sensitive to high temperatures (37 °C) in this system (Fig. 3*D*, panel 5), and the L > P and ΔE5 variants were slightly sensitive to low temperatures (17 °C and 23 °C) (Fig. 3*D*, panels 2 and 3).

Similarly, we probed the ability of human WT and variant RBM28 to complement Nop4 depletion in yeast. Again, coexpression of endogenous Nop4 with the RBM28 constructs did not alter normal vegetative growth at 30 °C (Fig. 3*D*, panel 6). Mirroring the Nop4 constructs, the WT, L > P, and ΔE5 RBM28 proteins supported growth in the absence of endogenous Nop4 at 23 °C and 30 °C (Fig. 3*D*, panels 8 and 9). These variants also had increasingly limited ability to complement Nop4 depletion at 17 °C (Fig. 3*D*, panel 7). EV and ΔE8 RBM28 failed to rescue growth at all temperatures examined (Fig. 3*D*, panels 6–10). Surprisingly, baseline WT RBM28 complementation was significantly impaired at 37 °C (Fig. 3*D*, panel 10), suggesting that human RBM28 sequence or structure may have diverged enough from Nop4 to fail to effectively complement Nop4 at 37 °C. WT RBM28 was the only RBM28 construct to rescue some growth at 37 °C, indicating RBM28 variant proteins have impaired function compared to WT RBM28 (Fig. 3*D*, panel 10). The failure of RBM28 constructs to complement Nop4 depletion at 37 °C versus at 30 °C was not attributable to diminished protein expression levels, as the expression of each protein was comparable at both 30 °C and 37 °C (*SI Appendix*, Fig. S2*A*). However, we hypothesize that the lower expression of the RBM28 constructs compared to the Nop4 constructs (Fig. 3*C*, *Endogenous Nop4 OFF)* is due to suboptimal codon usage, limiting the potential for RBM28-mediated Nop4 complementation in this system. We conclude that the variant constructs for Nop4 and RBM28 rescue growth in our yeast model to differing degrees.

To verify these results, we collected growth curve data at absorbance OD_{600} using an automated plate reader (*SI Appendix*, Fig. S2 *B* and *C* and Dataset S3) and calculated the maximum growth rate for each strain (Fig. 3*E*). We found that within either the Nop4 or RBM28 construct family, the WT construct was the fittest, while the corresponding L > P and ΔE5 constructs were hypomorphic and the corresponding ΔE8 construct matched the growth of the null EV strain (Fig. 3*E* and *SI Appendix*, Fig. S2 *B* and *C*) at both 30 °C and 37 °C. As before, RBM28 strains demonstrated stark failure to complement the endogenous Nop4

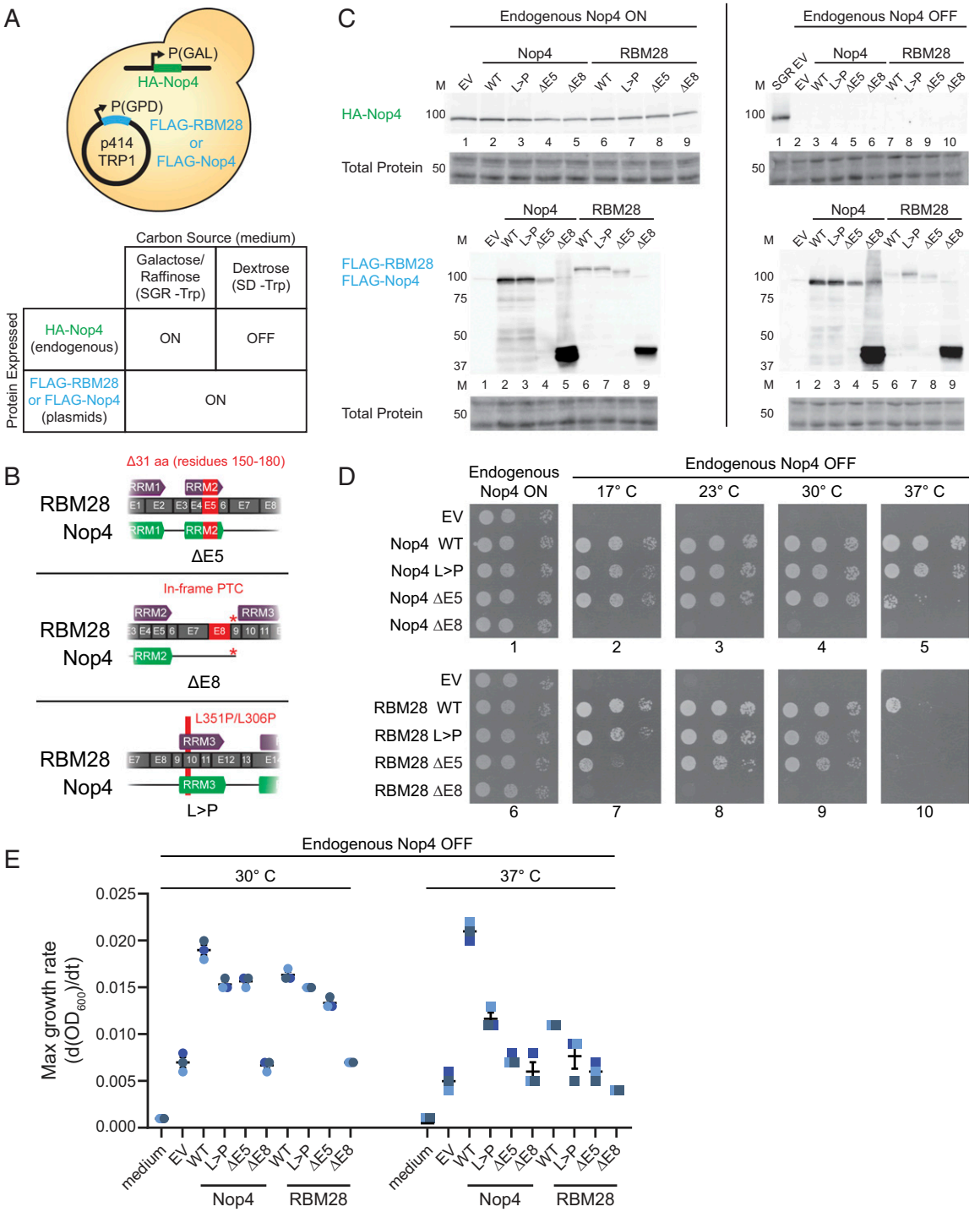

Fig. 3. Variant Nop4 and RBM28 inhibit vegetative growth in a yeast model. (*A*) Diagram of yeast model containing endogenous HA-tagged Nop4 under a repressible P(GAL) promoter (green) with plasmid-borne constitutively expressed FLAG-tagged versions of Nop4 or RBM28 (blue). Endogenous HA-Nop4 is produced in SGR -Trp but repressed in SD -Trp; conversely, FLAG-Nop4 or FLAG-RBM28 is expressed in both conditions. (*B*) Diagrams of patient variant protein constructs for RBM28 or Nop4. ΔE5, exon 5 variant; ΔE8, exon 8 variant; L > P, classical Leu > Pro variant [p.(Leu306Pro) in Nop4, p.(Leu351Pro) in *RBM28*]. Modifications of the WT construct for each variant are noted in red. Letters aa indicate amino acids; PTC (*) indicates premature termination codon. (*C*) Biochemical validation of the yeast model via immunoblotting. Strains were grown to log phase in liquid SGR -Trp (*Left*) or SD -Trp (*Right*) and protein was harvested for immunoblot analysis of either HA- or FLAG-tagged species. Note the presence of a faint, unrelated cross-reacting band present in all lanes around 100 kDa. Total protein loading controls were imaged for each blot. M, protein ladder size marker. (*D*) Tenfold serial dilutions of each yeast strain were grown on SGR -Trp at 30 °C (*Left*) or SD -Trp between 17 and 37 °C (*Right*). Strains were grown between 3 and 12 d, depending on temperature. EV indicates empty vector. L > P indicates Leu to Pro mutation [p.(Leu306Pro) in Nop4, p.(Leu351Pro) in *RBM28*]. ΔE5 and ΔE8 indicate proteins resulting from deletion of exon 5 or exon 8 respectively. (*E*) Summary of the maximum growth rate attained by each strain using OD_{600} absorbance from an automated plate reader. Strains were grown in triplicate for 24 h at either 30 °C (*Left*) or 37 °C (*Right*) in SD -Trp (Endogenous Nop4 OFF). Individual values per experiment are overlaid on the mean +/− SEM. Data were analyzed using two-way ANOVA followed by Tukey's multiple comparisons test with all possible comparisons within each temperature family. The ANOVA table and multiple comparison statistical analyses are included in Dataset S3.

at 37 °C. Altogether, our serial dilution results on plates and growth curve results in liquid culture indicate that ultimately, each variant cannot rescue growth as well as its WT counterpart in the absence of endogenous Nop4 across all temperatures tested; in particular, both ΔE8 variants completely fail to rescue growth.

Finally, we assayed the ability of each protein construct to rescue RB in the absence of endogenous Nop4. Given Nop4's established roles in early endonucleolytic cleavage of the pre-rRNA precursor, mature 25S rRNA biogenesis, and as a hub protein in the LSU processome (34, 36–38, 56), we hypothesized that the patient variant proteins would only partially rescue levels of mature 25S rRNA and pre-rRNA precursor intermediates. In particular, we expected that the 35S primary pre-rRNA transcript would accumulate at the expense of large subunit rRNAs in precursor (27S, 7S) or mature (25S) form (Fig. 4*A*), as previously observed (34, 36, 37, 56).

Harnessing a previously successful strategy for examining hypomorphic alleles (34), we depleted each strain of endogenous HA-Nop4 for 48 h at 23 °C, after which total RNA was isolated and purified. Using methylene blue staining for mature rRNAs, we observed that the 25S/18S rRNA ratios remained unchanged in the presence of endogenous Nop4 (Fig. 4*B*, odd-numbered lanes). In contrast, we found sharp decreases in the 25S/18S ratios for the EV, the null ΔE8 Nop4, and null ΔE8 RBM28 variant proteins, indicating that they are unable to fully complement Nop4's role in mature 60S rRNA production (Fig. 4*B*, lanes 2, 10, and 18).

We probed the extent to which pre-rRNA processing was interrupted upon complementation of Nop4 depletion by each variant protein. Northern blots using the internal transcribed spacer 2 (ITS2) probe Oligo E (Fig. 4*A*) revealed that pre-rRNA processing intermediate accumulation was not disrupted in a dominant negative manner when endogenous Nop4 and extrachromosomal protein constructs are coexpressed, consistent with our growth and mature rRNA assays (Fig. 4*C*, odd-numbered lanes). However, we observed abnormal accumulation of pre-rRNA processing intermediates for all protein variants compared to WT Nop4. Specifically, steady-state levels of the 27S precursor decreased relative to the 35S primary transcript, consistent with the previously reported importance of Nop4 in early internal transcribed spacer 1 (ITS1) cleavage (Fig. 4*C*, even-numbered lanes) (34, 36, 37, 56). Compared to WT Nop4, the Nop4 variants all yielded decreased 27S/35S ratios on Northern blots. Interestingly, WT human RBM28 only partially rescued pre-rRNA processing compared to Nop4 WT (Fig. 4*C*, lane 12); however, the RBM28 variants also exhibited decreased 27S/35S ratios compared to RBM28 WT (Fig. 4*C*, lanes 14, 16, and 18). Thus, while L > P and ΔE5 constructs were able to rescue growth and mature rRNA production, these mutants failed to completely rescue pre-rRNA processing according to the more sensitive Northern blotting assay.

We also examined 7S RNA precursor levels relative to the 35S primary transcript. While mean 7S/35S ratios for all mutants and WT RBM28 decreased by 20 to 80% compared to Nop4 WT, these comparisons were not statistically significant due to high variability from three outlier measurements (*SI Appendix*, Fig. S3*A*). Additionally, stark failure of WT and variant human RBM28 to rescue 7S RNA precursor levels indicates that RBM28 cannot complement in the C_2 cleavage step in ITS2 (Fig. 4 *A* and *C* and *SI Appendix*, Fig. S3*A*). Together, these data demonstrate that patient variants of Nop4 and RBM28 cause aberrant large subunit pre-rRNA processing and, in the most severe cases, significantly impair LSU biogenesis and growth of yeast.

Discussion

This is the second family with ANE syndrome, a rare ribosomopathy, reported to date and a significant case of ANE syndrome in a female pediatric patient. ANE syndrome is caused by defects in the essential 60S assembly factor RBM28 (Nop4 in yeast). This ANE syndrome patient has a clinical presentation that is similar to that observed in the initial presentation of the disease (31) but harbors a molecular pathology featuring deleterious biallelic splicing variants affecting two different exons of the *RBM28* gene. In silico and in vivo experiments demonstrate that the ΔE5 variant results in a hypomorphic partial deletion in the RRM2 domain of RBM28, while the ΔE8 variant creates a premature stop resulting in a functionally null transcript. Both variants result in reduced growth and aberrant 60S-specific pre-rRNA processing in yeast, consistent with RBM28's known essential role as a 60S assembly factor. The identification of a second occurrence of ANE syndrome underscores the important role of the nucleolar RBM28 protein in maintaining human health and normal development.

This ANE syndrome patient broadly shares a clinical presentation and a recessive genetic etiology of disease with the first ANE syndrome case report (31), while her specific genetic pathology featuring biallelic splicing variants differs significantly. Consistent with the established definition of ANE syndrome (31, 35), this patient's clinical features include alopecia, craniofacial defects, hypoplastic pituitary, and hair and skin defects. Unlike the previous ANE syndrome patients (31, 32), hormonal irregularities were not observed, although they may develop closer to the pubertal transition given the presence of a hypoplastic pituitary. Both sets of cases are caused by recessive genetic variants in *RBM28*, a 60S assembly factor crucial for mature 28S rRNA production. However, while the previous ANE syndrome patients are homozygous for the RBM28 p.(Leu351Pro) (L > P) missense variant, this patient possesses compound heterozygous 5′ splice site variants at ΔE5 and ΔE8 of *RBM28*. Additionally, one of the patient's unaffected parents bears the null ΔE8 allele, demonstrating that ANE syndrome is not a disease of haploinsufficiency. Like Shwachman–Diamond syndrome (26) and Bowen–Conradi syndrome (14, 57), which are caused by recessive variants in the assembly factors SBDS and EMG1 respectively, ANE syndrome has an autosomal recessive pathology that contrasts with well-described dominant haploinsufficient ribosomopathies such as DBA and 5q- syndrome (12, 13, 18, 21).

The finding that RBM28 function is impaired by both the ΔE5 and ΔE8 variants is in line with the biochemical role of RBM28 (human) and Nop4 (yeast) in RB (34, 36–40). Consistent with the discovery that the ANE patient's ΔE5 allele is hypomorphic for growth and 60S pre-rRNA processing, mutation of the Nop4 RRM2 RNP1 RNA binding motif causes reduced 60S subunit levels and impaired polysome formation (38). Likewise, nullity of the ΔE8 allele in RBM28 is consistent with the previous finding (34, 38) that the C-terminal half of Nop4 containing RRM3, RRM4, and the carboxyl terminus is essential. Moreover, transcripts from the ΔE8 allele will contain a PTC and are likely degraded by NMD after a pioneer round of translation, which increases the likelihood that this allele is null. In combination, these alleles comprise the molecular basis of this patient's ANE syndrome pathology.

We observe only subtle differences in yeast growth between WT and the hypomorphic L > P or ΔE5 variants even at reduced temperatures at which RB is restrictive. Although one might expect hypomorphic variants of an essential ribosome assembly factor to yield greater impairment in growth, we emphasize that when coupled with the null ΔE8 allele in the ANE patient, the hypomorphic ΔE5 variant retains enough residual function to support life. This result underscores that partially functional—but not completely null—mutations in *RBM28* are a hallmark of ANE syndrome.

While several yeast pre-60S cryogenic electron microscopy (cryo-EM) structural models are now available (58–60), Nop4 is conspicuously absent in them, perhaps due to the transient nature of its interaction as demonstrated by proteomics experiments (61). Failure to localize Nop4 in pre-60S structures obscures its direct in vivo RNA and protein interactions,

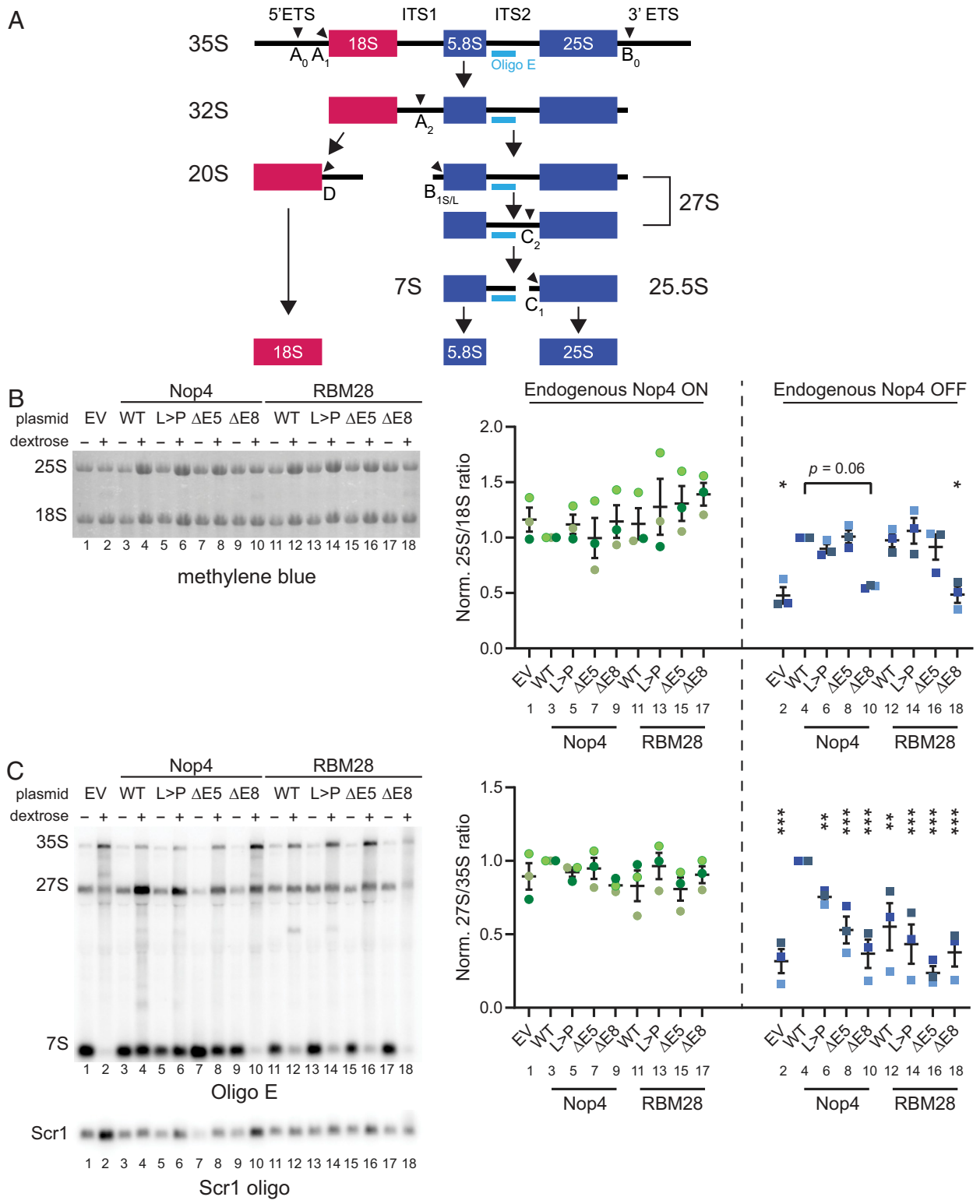

Fig. 4. Nop4 and RBM28 variants fail to rescue mature 25S production and preribosomal RNA processing in ITS2. (*A*) Diagram of preribosomal RNA (pre-rRNA) processing in *Saccharomyces cerevisiae*. The 35S primary transcript undergoes endonucleolytic cleavage steps (arrowheads) and exonuclease trimming to render three of the four mature rRNAs. Nonfunctional spacer regions (external transcribed spacer [ETS], and internal transcribed spacer [ITS]) and prerRNA intermediates are labeled. The small subunit 18S rRNA is shown in red, while the large subunit 5.8S and 28S rRNAs are shown in dark blue. Oligo E is shown in light blue next to every intermediate detected by Oligo E via Northern blot. (*B* and *C*) Methylene blue staining of mature rRNAs (*B*) and Northern blotting of pre-rRNA intermediates detected by Oligo E (*C*). A total of 3 μg RNA from each strain was run side-by-side for samples with endogenous Nop4 ON or OFF (– or + dextrose, respectively). Blotting for Scr1 serves as a loading control for the Northern blot. Quantification of three experiments is presented on the right. 25S/18S ratio is calculated in *B*, and 27S/35S ratio is calculated in *C*. Values are normalized to Nop4 WT for each endogenous Nop4 level. Individual values per experiment are overlaid on the mean $^{+/-}$ SEM. Data were analyzed by repeated measures using two-way ANOVA followed by Dunnett's post hoc test with comparison to Nop4 WT for each media condition. $P < 0.05$ (*), $P < 0.01$ (**), $P < 0.001$ (***).

precluding structural insight into how ANE syndrome genetic variants interfere with normal Nop4 RNA binding and hub protein functions. In addition to affinity purification of early pre-60S particles, cryo-EM methods utilizing cross-linking (62, 63) or powerful in silico purification (64, 65) may enable localization of Nop4 and its contact partners in the pre-LSU complex. Careful mutational studies could also reveal the structural consequences of ANE syndrome variants on LSU biogenesis. Additional structural studies of early pre-60S particles containing Nop4 will more fully define Nop4's role in RB and the structural consequences of ANE syndrome genetic variants.

In the future, we anticipate that identification of additional cases of ANE syndrome and realization of more advanced models of disease will facilitate better understanding of the pathophysiology of ANE syndrome. As awareness increases about rare diseases affecting RB and as exome or genome sequencing bears more fruit in the clinic, additional cases of ANE syndrome will likely be identified. As in our study, modeling variants of uncertain significance in biological systems will continue to aid in variant classification. Furthermore, since the study of ANE syndrome variants in a strictly cellular context cannot directly reveal the neurological and developmental consequences of the disease, investigating *RBM28* variants in animal models will illuminate how brain development is differentially impaired by each of the three known ANE syndrome variants. Additional clinical and basic scientific studies will allow us to better grasp the developmental consequences of ANE syndrome and its underlying molecular mechanisms.

Materials and Methods

Patient Evaluation. The patient in this report was 2 y old at the start of data collection. She was evaluated by specialists in clinical genetics, endocrinology, dermatology, pediatric neurology, phonoaudiology, and physical therapy at the Teaching Hospital of the Federal University of Pelotas, Brazil. She underwent complementary clinical diagnostic tests including pituitary hormonal evaluation and two brain MRIs at ages 4 and 6 y. Molecular diagnosis was obtained by clinical exome sequencing. A hair sample was analyzed by electron microscopy. The patient's family signed study approvals for all testing and for the publication of this report. The present study was approved by the institutional review board of Federal University of Pelotas.

In Silico Splicing Prediction Algorithms. Web interfaces for HumanSplicingFinder [HSF (47)] and AnalyzerSpliceTool (48) were used to calculate the severity of each *RBM28* patient variant. SpliceAI (44) was run from a command line in a UNIX environment to evaluate the strength of a splice site. The COSSMO web interface (50) was used to identify possible splice sites that could substitute for the patient's defective WT splice sites. Analyses were executed for the splice acceptors of exon 6 and exon 9.

Oligonucleotide Design and Synthesis; Sequencing. All primer oligonucleotides for cloning and sequencing were designed in the Geneious Prime software package (version 2019.0.4, Biomatters, Ltd.) and prepared by Yale Keck Oligonucleotide Synthesis. DNA sequencing was performed by GENEWIZ.

Image Acquisition and Analysis. Images of agarose gels were acquired on an Alpha Innotech AlphaImager 2200. Chemiluminescent immunoblots and methylene blue–stained RNA blots were imaged with a Bio-Rad ChemiDoc, and radiolabeled RNA blots were imaged with an Amersham Typhoon IP Biomolecular Imager. Image quantification of gels and blots was conducted with ImageJ version 1.51j8. All quantifications were made using unaltered, uncompressed original image files. Entire images presented in the manuscript may be adjusted for lightness or contrast for better clarity and consistency. No data were obscured by such processing. All data analysis was conducted on unaltered raw images.

Molecular Cloning and Plasmid Preparation. Minigene fragments were cloned into the empty pcDNA5/FRT/TO vector from the RP11-640G20 clone of the RPCI-11 Human Male bacterial artificial chromosome library (BACPAC Genomics). Primers spanning exon 4 to exon 6, exon 7 to exon 9, and exon 1 to exon 6 (Dataset S2) were used to amplify DNA by PCR with Q5 High-Fidelity DNA Polymerase (New England Biolabs M0491S). Amplicons were restriction endonuclease cloned into pcDNA5/FRT/TO empty vector (KpnI-HF and NotI-HF, New England Biolabs). Site-directed mutagenesis was carried out via PCR with Q5 DNA polymerase and partially overlapping mutagenic primers (66) (Dataset S2) to introduce patient mutations into the wild-type minigene constructs.

Coding sequences for wild-type or L > P versions of Nop4 [p.(Leu306Pro)] or RBM28 (34) [p.(Leu351Pro)] were shuttled into the p414GPD-3xFLAG vector. Gibson cloning was used to generate ΔE5 and ΔE8 deletion plasmids for RBM28 directly or for Nop4 by alignment and rational design in Geneious. Constructs were verified by DNA sequencing.

Mammalian Minigene Splicing Assays. Flp-In T-REx HEK293 cells (Invitrogen R75007) were a generous gift from P. Gallagher, Yale School of Medicine, New Haven, CT. Cells were grown in DMEM (Gibco 11965092) with 10% fetal bovine serum (Gibco 16050122) and 15 μg/mL blasticidin S (Alfa Aesar J67216XF) and were incubated at 37 °C in a humidified atmosphere with 5% CO_2. To genomically integrate each minigene construct, cells were transfected with OptiMEM (Gibco 31985070), Lipofectamine 3000 (Invitrogen L3000015), and a 9:1 mass ratio of pOG44:pcDNA5/FRT/TO vectors according to the manufacturer's protocol. Approximately 11.6 μg pOG44 and 1.3 μg pcDNA5/FRT/TO were used to transfect cells in 10cm dishes with each minigene construct. Cells were split to less than 25% confluency, and 200 μg/mL hygromycin B (Gibco 10687010) was introduced to the media for selection. Selective media was changed every 2 d until confluency, at which point polyclonal populations were harvested. Genomic DNA was isolated from each line with DNeasy Blood & Tissue kits (QIAGEN 69504), PCR amplified, and sequenced to validate transfection and integration.

To isolate total RNA, clonal cell lines were seeded in 6-well plates, and 1 μg/mL tetracycline was added after 24 h to induce minigene transcription. After 48 h, total RNA was harvested using TRIzol (Invitrogen 15596018). Complementary DNA (cDNA) was synthesized from 1 μg total RNA using random hexamer primers with the iScript cDNA synthesis kit (Bio-Rad 1708890). cDNA was PCR amplified using Taq DNA Polymerase with ThermoPol buffer (New England Biolabs M0267S) using primers located in Dataset S2. The reaction products were separated on a 1.0% agarose gel containing ethidium bromide. For DNA sequencing, products were column purified; single-band products were sequenced directly while products with multiple bands were TOPO-TA cloned before sequencing (Invitrogen 450030).

Yeast Growth Media, Transformation, Serial Dilutions, and Automated Growth Curve Collection. Yeast-peptone media supplemented with 2% (wt/vol) dextrose or 1% (wt/vol) galactose/1% (wt/vol) raffinose was used to grow YPH499 and *P(GAL)::3HA-NOP4* strains (34). Minimal media with either dextrose or galactose/raffinose sugar sources were supplemented with -Trp dropout mix to grow strains transformed with p414-GPD vectors (Takara Bio USA 630411, 630420, and 630413). Dextrose -Trp media is abbreviated as SD -Trp and galactose/raffinose -Trp media is abbreviated as SGR -Trp. Strains were depleted of endogenous HA-tagged Nop4 by first growing liquid cultures to log phase in SGR -Trp at 30 °C and then starting SD -Trp cultures for depletion of HA-Nop4 using a 1:100 dilution of the SGR -Trp culture. Cultures were grown for 24 h at 30 °C or 37 °C and 48 h at 23 °C. Cells were harvested for protein or RNA isolation in log phase, in which OD_{600} was between 0.2 and 0.8.

A previously constructed *P(GAL)::3HA-NOP4* background strain generated from a YPH499 parental strain (34) was transformed with p414-GPD plasmids containing Nop4 and RBM28 variants described above. The high-efficiency transformation protocol described by Gietz (67) was utilized to transform the background strain.

Tenfold serial dilutions to test growth were performed as previously described (34).

To collect growth curve data, a saturated culture of each strain was pelleted, washed with ddH_2O, resuspended in ddH_2O, measured at a 1:100 dilution at OD_{600} on a spectrophotometer, and diluted to 0.1 OD_{600} in either SGR -Trp or SD -Trp. The inner wells of a sterile 96-well microplate (Greiner Bio-One 655185, wells B2 to G11) were inoculated with 200 μL medium or diluted yeast strain in technical triplicate for each medium condition, and sterile water was used to fill the outside perimeter wells to prevent medium evaporation. The lidded microplate was loaded onto a BioTek Synergy H1 Hybrid Multi-Mode Microplate Reader set to maintain temperature at 30 °C or 37 °C as indicated, and whole-plate OD_{600} measurements were taken every 10 min for 24 h. Raw OD_{600} data were exported, and point-to-point OD_{600} differences were calculated in Excel as an approximation for the first-order derivative. Maximum growth rates for each strain replicate were calculated from these derivative calculations in JMP Pro-15, and data were graphed and analyzed by two-way ANOVA with Tukey's multiple comparisons test in GraphPad Prism 8.

Protein Isolation and Analysis. Total protein was isolated from yeast cells as previously described (68). Briefly, 15 mL of yeast in log phase (OD_{600} between 0.2 and 0.8) was harvested, centrifuged, washed in 1 mL ddH_2O, and resuspended in 1 mL cold 1.0 M lithium acetate on ice for 5 min. Cells were centrifuged again and lysed in 1 mL cold 400 mM sodium hydroxide on ice for 5 min. Cells were pelleted and all supernatant was removed before resuspension in 100 μL of 2.5X SDS loading buffer. Protein was boiled at 95 °C for 3 min, centrifuged at maximum speed, and loaded onto a gel or frozen at −20 °C. Handcast 8% SDS-PAGE gels containing 0.5% (vol/vol) trichloroethanol (Acros Organics 139441000) were used to separate total protein at 110 V for 2 h. Total protein was imaged using the ChemiDoc stain-free imaging protocol (Bio-Rad) to ensure even loading at the gel stage. Following membrane transfer with the Trans-Blot Turbo system (Bio-Rad), blots were imaged again for total protein without crosslinking to ensure transfer quality; these images are presented as blot loading controls. Immunoblotting was carried out using 5% (wt/vol) Omniblok dry milk (American Bio AB10109) in phosphate-buffered saline/Tween (PBST, pH = 7.1, 5% [vol/vol] Tween) with 1:30,000 Monoclonal ANTI-FLAG M2-Peroxidase (HRP) (Sigma A8592) or 1:2,000 mouse anti-HA (clone 12CA5) followed by 1:10,000 sheep peroxidase–linked anti-mouse IgG (GE Healthcare NXA931V).

RNA Isolation and Analysis. Human cell line total RNA isolation is described above. RNA was isolated from yeast cells following the protocol of Shedlovskiy, et al. (69) after depletion of endogenous HA-Nop4 (see *Materials and Methods*). Briefly, 15 mL of yeast in log phase (OD_{600} between 0.2 and 0.8) were washed in ddH_2O and pelleted, then resuspended in 400 μL formamide/EDTA, consisting of 98% (vol/vol) formamide and 2% (vol/vol) 0.5 M EDTA. Yeast were incubated for at least 10 min at 70 °C and vortexed for 10 s before pelleting and supernatant collection. Extracted RNA was precipitated with 3 M sodium acetate and washed thrice with 75% ethanol. A total of 3 μg of purified total RNA was separated on a denaturing formaldehyde agarose gel, transferred to a Hybond-XL membrane (GE Healthcare), methylene blue–stained and imaged, and blotted with radiolabeled Oligo E or Scr1 as previously described (34).

Data Availability. All study data are included in the article and/or supporting information.

ACKNOWLEDGMENTS. We thank the patient's family for accepting being included in this study. We also thank the members of the laboratory of S.J.B. for insightful information, questions, and comments throughout the manuscript writing process, and P. Gallagher for reagents and helpful suggestions for the minigene experiments. We thank F. Isaacs, Z. Liang, F. Radford, L. Quinto, J. Gallagher, and S. Chin-Bow for their gracious advice and assistance with collecting growth curve data on automated plate readers. We thank Jonatas Favero Prietto and Marjana Reis Lima for reviewing the brain MRI images. S.J.B. acknowledges 1R35GM131687 from NIH for support of her laboratory. C.J.B. and S.J.B. acknowledge NIH T32GM007223 for funding. No NIH funding was used for patient examination, evaluation, or clinical sequencing.

1. J. L. Woolford Jr, S. J. Baserga, Ribosome biogenesis in the yeast Saccharomyces cerevisiae. *Genetics* **195**, 643–681 (2013).
2. A. K. Henras, C. Plisson-Chastang, M. F. O'Donohue, A. Chakraborty, P. E. Gleizes, An overview of pre-ribosomal RNA processing in eukaryotes. *Wiley Interdiscip. Rev. RNA* **6**, 225–242 (2015).
3. P. Nerurkar *et al*., Eukaryotic ribosome assembly and nuclear export. *Int. Rev. Cell Mol. Biol.* **319**, 107–140 (2015).
4. R. N. Nazar, Ribosomal RNA processing and ribosome biogenesis in eukaryotes. *IUBMB Life* **56**, 457–465 (2004).
5. T. Moss, F. Langlois, T. Gagnon-Kugler, V. Stefanovsky, A housekeeper with power of attorney: The rRNA genes in ribosome biogenesis. *Cell. Mol. Life Sci.* **64**, 29–49 (2007).
6. I. G. Wool, Y. L. Chan, A. Glück, Structure and evolution of mammalian ribosomal proteins. *Biochem. Cell Biol.* **73**, 933–947 (1995).
7. N. Ban *et al*., A new system for naming ribosomal proteins. *Curr. Opin. Struct. Biol.* **24**, 165–169 (2014).
8. J. R. Warner, The economics of ribosome biosynthesis in yeast. *Trends Biochem. Sci.* **24**, 437–440 (1999).
9. J. D. Lewis, D. Tollervey, Like attracts like: Getting RNA processing together in the nucleus. *Science* **288**, 1385–1389 (2000).
10. E. V. Schmidt, The role of c-myc in cellular growth control. *Oncogene* **18**, 2988–2996 (1999).
11. K. I. Farley-Barnes, L. M. Ogawa, S. J. Baserga, Ribosomopathies: Old concepts, new controversies. *Trends Genet.* **35**, 754–767 (2019).
12. A. Narla, B. L. Ebert, Ribosomopathies: Human disorders of ribosome dysfunction. *Blood* **115**, 3196–3205 (2010).
13. E. W. Mills, R. Green, Ribosomopathies: There's strength in numbers. *Science* **358**, eaan2755 (2017).
14. S. B. Sondalle, S. J. Baserga, Human diseases of the SSU processome. *Biochim. Biophys. Acta* **1842**, 758–764 (2014).
15. K. L. McCann, S. J. Baserga, Genetics. Mysterious ribosomopathies. *Science* **341**, 849–850 (2013).
16. A. P. Ross, K. S. Zarbalis, The emerging roles of ribosome biogenesis in craniofacial development. *Front. Physiol.* **5**, 26 (2014).
17. P. C. Yelick, P. A. Trainor, Ribosomopathies: Global process, tissue specific defects. *Rare Dis.* **3**, e1025185 (2015).
18. L. Da Costa, T. Leblanc, N. Mohandas, Diamond-Blackfan anemia. *Blood* **136**, 1262–1273 (2020).
19. H. T. Gazda *et al*., Mutations of the genes for ribosomal proteins l5 and l11 are a common cause of diamond-blackfan anemia. *Blood* **110**, 130a–131a (2007).
20. H. T. Gazda *et al*., Ribosomal protein L5 and L11 mutations are associated with cleft palate and abnormal thumbs in Diamond-Blackfan anemia patients. *Am. J. Hum. Genet.* **83**, 769–780 (2008).
21. J. Boultwood, A. Pellagatti, J. S. Wainscoat, Haploinsufficiency of ribosomal proteins and p53 activation in anemia: Diamond-Blackfan anemia and the 5q- syndrome. *Adv. Biol. Regul.* **52**, 196–203 (2012).
22. J. C. Ulirsch *et al*., The genetic landscape of Diamond-Blackfan Anemia. *Am. J. Hum. Genet.* **103**, 930–947 (2018).
23. Y. Wan *et al*., Transcriptome analysis reveals a ribosome constituents disorder involved in the RPL5 downregulated zebrafish model of Diamond-Blackfan anemia. *BMC Med. Genomics* **9**, 13 (2016).
24. N. Burwick, A. Shimamura, J. M. Liu, Non-Diamond Blackfan anemia disorders of ribosome function: Shwachman Diamond syndrome and 5q- syndrome. *Semin. Hematol.* **48**, 136–143 (2011).
25. T. L. Levin, O. Mäkitie, W. E. Berdon, R. S. Lachman, Shwachman-Bodian-Diamond syndrome: Metaphyseal chondrodysplasia in children with pancreatic insufficiency and neutropenia. *Pediatr. Radiol.* **45**, 1066–1071 (2015).
26. A. J. Warren, Molecular basis of the human ribosomopathy Shwachman-Diamond syndrome. *Adv. Biol. Regul.* **67**, 109–127 (2018).
27. B. C. Valdez, D. Henning, R. B. So, J. Dixon, M. J. Dixon, The Treacher Collins syndrome (TCOF1) gene product is involved in ribosomal DNA gene transcription by interacting with upstream binding factor. *Proc. Natl. Acad. Sci. U.S.A.* **101**, 10709–10714 (2004).
28. B. Gonzales *et al*., The Treacher Collins syndrome (TCOF1) gene product is involved in pre-rRNA methylation. *Hum. Mol. Genet.* **14**, 2035–2043 (2005).
29. J. G. Dauwerse *et al*., Mutations in genes encoding subunits of RNA polymerases I and III cause Treacher Collins syndrome. *Nat. Genet.* **43**, 20–22 (2011).
30. K. N. Weaver *et al*., Acrofacial dysostosis, Cincinnati type, a mandibulofacial dysostosis syndrome with limb anomalies, is caused by POLR1A dysfunction. *Am. J. Hum. Genet.* **96**, 765–774 (2015).
31. J. Nousbeck *et al*., Alopecia, neurological defects, and endocrinopathy syndrome caused by decreased expression of RBM28, a nucleolar protein associated with ribosome biogenesis. *Am. J. Hum. Genet.* **82**, 1114–1121 (2008).
32. R. Spiegel, S. A. Shalev, A. Adawi, E. Sprecher, Y. Tenenbaum-Rakover, ANE syndrome caused by mutated RBM28 gene: A novel etiology of combined pituitary hormone deficiency. *Eur. J. Endocrinol.* **162**, 1021–1025 (2010).
33. E. Warshauer *et al*., RBM28, a protein deficient in ANE syndrome, regulates hair follicle growth via miR-203 and p63. *Exp. Dermatol.* **24**, 618–622 (2015).
34. K. L. McCann, T. Teramoto, J. Zhang, T. M. Tanaka Hall, S. J. Baserga, The molecular basis for ANE syndrome revealed by the large ribosomal subunit processome interactome. *eLife* **5**, e16381 (2016).
35. Online Mendelian Inheritance in Man, OMIM®. Johns Hopkins University, Baltimore, MD. MIM Number: 612079: 2015-02-06. https://omim.org/ (Accessed 26 April 2021).
36. T. Bergès, E. Petfalski, D. Tollervey, E. C. Hurt, Synthetic lethality with fibrillarin identifies NOP77p, a nucleolar protein required for pre-rRNA processing and modification. *EMBO J.* **13**, 3136–3148 (1994).
37. C. Sun, J. L. Woolford Jr, The yeast NOP4 gene product is an essential nucleolar protein required for pre-rRNA processing and accumulation of 60S ribosomal subunits. *EMBO J.* **13**, 3127–3135 (1994).
38. C. Sun, J. L. Woolford Jr, The yeast nucleolar protein Nop4p contains four RNA recognition motifs necessary for ribosome biogenesis. *J. Biol. Chem.* **272**, 25345–25352 (1997).
39. S. Granneman, E. Petfalski, D. Tollervey, A cluster of ribosome synthesis factors regulate pre-rRNA folding and 5.8S rRNA maturation by the Rat1 exonuclease. *EMBO J.* **30**, 4006–4019 (2011).
40. K. L. McCann, J. M. Charette, N. G. Vincent, S. J. Baserga, A protein interaction map of the LSU processome. *Genes Dev.* **29**, 862–875 (2015).
41. S. Richards *et al*.; ACMG Laboratory Quality Assurance Committee, Standards and guidelines for the interpretation of sequence variants: A joint consensus recommendation of the American College of Medical Genetics and Genomics and the Association for Molecular Pathology. *Genet. Med.* **17**, 405–424 (2015).
42. I. A. Adzhubei *et al*., A method and server for predicting damaging missense mutations. *Nat. Methods* **7**, 248–249 (2010).
43. R. Vaser, S. Adusumalli, S. N. Leng, M. Sikic, P. C. Ng, SIFT missense predictions for genomes. *Nat. Protoc.* **11**, 1–9 (2016).
44. K. Jaganathan *et al*., Predicting splicing from primary sequence with deep learning. *Cell* **176**, 535–548.e24 (2019).

45. K. J. Karczewski *et al*.; Genome Aggregation Database Consortium, The mutational constraint spectrum quantified from variation in 141,456 humans. *Nature* **581**, 434–443 (2020).
46. M. B. Shapiro, P. Senapathy, RNA splice junctions of different classes of eukaryotes: Sequence statistics and functional implications in gene expression. *Nucleic Acids Res.* **15**, 7155–7174 (1987).
47. F. O. Desmet *et al*., Human Splicing Finder: An online bioinformatics tool to predict splicing signals. *Nucleic Acids Res.* **37**, e67 (2009).
48. I. Carmel, S. Tal, I. Vig, G. Ast, Comparative analysis detects dependencies among the 5′ splice-site positions. *RNA* **10**, 828–840 (2004).
49. M. G. Reese, F. H. Eeckman, D. Kulp, D. Haussler, Improved splice site detection in Genie. *J. Comput. Biol.* **4**, 311–323 (1997).
50. H. Bretschneider, S. Gandhi, A. G. Deshwar, K. Zuberi, B. J. Frey, COSSMO: Predicting competitive alternative splice site selection using deep learning. *Bioinformatics* **34**, i429–i437 (2018).
51. T. Wang *et al*., Identification and characterization of essential genes in the human genome. *Science* **350**, 1096–1101 (2015).
52. R. M. Meyers *et al*., Computational correction of copy number effect improves specificity of CRISPR-Cas9 essentiality screens in cancer cells. *Nat. Genet.* **49**, 1779–1784 (2017).
53. Broad Institute, Data from DepMap 20Q2 Public Dataset. *Figshare*. Available at https://doi.org/10.6084/m9.figshare.12280541.v4. Deposited 4 June 2020.
54. A. G. Fernandez *et al*., New genes with roles in the C. elegans embryo revealed using RNAi of ovary-enriched ORFeome clones. *Genome Res.* **15**, 250–259 (2005).
55. C. Guthrie, H. Nashimoto, M. Nomura, Structure and function of E. coli ribosomes. 8. Cold-sensitive mutants defective in ribosome assembly. *Proc. Natl. Acad. Sci. U.S.A.* **63**, 384–391 (1969).
56. H. Qiu *et al*., Identification of genes that function in the biogenesis and localization of small nucleolar RNAs in Saccharomyces cerevisiae. *Mol. Cell. Biol.* **28**, 3686–3699 (2008).
57. A. S. Warda *et al*., Effects of the Bowen-Conradi syndrome mutation in EMG1 on its nuclear import, stability and nucleolar recruitment. *Hum. Mol. Genet.* **25**, 5353–5364 (2016).
58. Z. A. Sanghai *et al*., Modular assembly of the nucleolar pre-60S ribosomal subunit. *Nature* **556**, 126–129 (2018).
59. L. Kater *et al*., Visualizing the assembly pathway of nucleolar pre-60S ribosomes. *Cell* **171**, 1599–1610.e14 (2017).
60. C. Ma *et al*., Structural snapshot of cytoplasmic pre-60S ribosomal particles bound by Nmd3, Lsg1, Tif6 and Reh1. *Nat. Struct. Mol. Biol.* **24**, 214–220 (2017).
61. G. Zisser *et al*., Viewing pre-60S maturation at a minute's timescale. *Nucleic Acids Res.* **46**, 3140–3151 (2018).
62. K. Adamus, S. N. Le, H. Elmlund, M. Boudes, D. Elmlund, AgarFix: Simple and accessible stabilization of challenging single-particle cryo-EM specimens through cross-linking in a matrix of agar. *J. Struct. Biol.* **207**, 327–331 (2019).
63. H. Stark, GraFix: Stabilization of fragile macromolecular complexes for single particle cryo-EM. *Methods Enzymol.* **481**, 109–126 (2010).
64. N. Fischer *et al*., The pathway to GTPase activation of elongation factor SelB on the ribosome. *Nature* **540**, 80–85 (2016).
65. A. B. Loveland, G. Demo, N. Grigorieff, A. A. Korostelev, Ensemble cryo-EM elucidates the mechanism of translation fidelity. *Nature* **546**, 113–117 (2017).
66. H. Liu, J. H. Naismith, An efficient one-step site-directed deletion, insertion, single and multiple-site plasmid mutagenesis protocol. *BMC Biotechnol.* **8**, 91 (2008).
67. R. D. Gietz, Yeast transformation by the LiAc/SS carrier DNA/PEG method. *Methods Mol. Biol.* **1205**, 1–12 (2014).
68. T. Zhang *et al*., An improved method for whole protein extraction from yeast Saccharomyces cerevisiae. *Yeast* **28**, 795–798 (2011).
69. D. Shedlovskiy, N. Shcherbik, D. G. Pestov, One-step hot formamide extraction of RNA from Saccharomyces cerevisiae. *RNA Biol.* **14**, 1722–1726 (2017).